Methane dry reforming on Ni loaded hydroxyapatite and fluoroapatite

Zouhair Boukha[a,b], Mohamed Kacimi[a], Manuel Fernando R. Pereira[b],

Joaquim L. Faria[b], José Luís Figueiredo[b], Mahfoud Ziyad[a,*]

[a] *Faculté des Sciences, Laboratoire de Physico-Chimie des Matériaux et Catalyse,*

Département de Chimie, Avenue lbn Battouta, B.P. 1014, Rabat, Morocco

[b] *Laboratório de Catálise e Materiais, Departamento de Engenharia Química, Faculdade de Engenharia,*

Universidade do Porto, Rua Dr. Roberto Frias, 4200-465 Porto, Portugal

* Corresponding author. ziyad@fsr.ac.ma

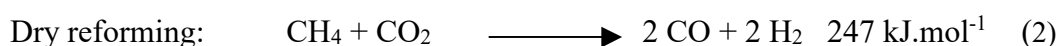Tel.: +212 37 77 56 34
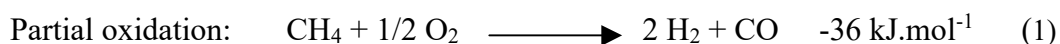
Fax: +212 37 77 56 34.

1

ABSTRACT

Calcium-hydroxyapatite and calcium-fluoroapatite loaded with different amounts of nickel were synthesized and characterized by several techniques including scanning electron microscopy, temperature programmed reduction (TPR), UV–visible–NIR and XPS spectroscopy. Three types of nickel species were detected in the two series of catalysts (i) Ni^{2+} ions exchanged with Ca^{2+} ions of the apatite framework. This Ni^{2+}/Ca^{2+} exchange seems to be restricted to nickel loadings inferior to 1 wt% Ni, (ii) small particles of NiO exhibiting strong interactions with the carriers (for x > 1 wt% Ni) and (iii) large particles of NiO which appear at high loadings. The distribution of the nickel between these three hosting sites depends on the nature of the apatite. For instance the amount of exchanged Ni^{2+} ions in Ni(1)/CaHAp is twice more important than in Ni(1)/CaFAp. The Ni(x)/CaHAp and Ni(x)/CaFAp catalysts were tested in methane dry reforming with CO_2. Methane conversion at 600 °C, increases with the nickel loading up to x = 4 where the activity is around the thermodynamic equilibrium (78%) and H_2/CO ratio close to 1. These results were confirmed by the investigation of the catalysts activity versus the temperature. Carbon deposition on the catalysts was found to also increase with nickel loading but without provoking any significant decay of the activity after 4 h on stream. The encouraging results achieved were attributed to the synergy between the basic properties of the apatites, their aptitude to chemisorb CO_2 and the catalytic features of the supported nickel.

1. Introduction

Natural gas is mainly used as a source of energy for industrial and domestic needs. It contains more than 80% of methane. The rest is made of heavier hydrocarbons, CO_2 and a complex mixture of pollutant gases. A major challenge of the chemical industry is to transform natural gas into ammonia, methanol, propanal, dimethyl ether or higher hydrocarbons (Fischer–Tropsch syntheses) via synthesis gas (H_2, CO) which is produced through the following catalytic processes:

$$\text{Partial oxidation:} \quad CH_4 + 1/2\ O_2 \longrightarrow 2\ H_2 + CO \quad \text{-36 kJ.mol}^{-1} \quad (1)$$

$$\text{Dry reforming:} \quad CH_4 + CO_2 \longrightarrow 2\ CO + 2\ H_2 \quad \text{247 kJ.mol}^{-1} \quad (2)$$

$$\text{Steam reforming:} \quad CH_4 + H_2O \longrightarrow CO + 3\ H_2 \quad \text{206 kJ.mol}^{-1} \quad (3)$$

In addition to carbon monoxide, these direct oxidative reactions produce hydrogen, which might be used in fuel cells and in the long term as fuel for non-polluting vehicles [1].

Dry reforming of methane with CO_2 compared to steam reforming has the advantage of consuming carbon dioxide which is known to be a greenhouse gas found in natural gas. However, the major drawback of this reforming process is the rapid deactivation of the catalyst due to carbon deposition on the active surface [2,3]. The conventional catalysts of reforming reactions generally contain noble metals (Ru, Pd, Pt, etc.) supported on oxides (SiO_2, Al_2O_3, ZrO_2, etc.) [4,5]. Transition metals such as Ni, and Co have also been investigated. They are active, less expensive than noble metals but very sensitive to poisoning probably because of their weak interactions with the support [6–9]. For this reason, search for new carriers capable of developing strong interactions with the loaded metal is essential [10–12]. Bradford et al. claimed selectivities in synthesis gas approaching 90% on nickel containing catalysts [13]. The literature reported that metallic nickel is more active than its oxide [14]. Moreover, when NiO is submitted to the reaction mixture ($CH_4 + CO_2$), it gets reduced into Ni without any alteration of the metal/support interactions but with a strong deposition of carbon on the catalyst provoking the decay of its activity [15,16].

The calcium-hydroxyapatite $Ca_{10}(PO_4)_6(OH)_2$ crystallizes in the hexagonal system and belongs to $P6_3/m$ point group [17,18]. Its framework can be described as a compact assemblage of Ca^{2+} ions and tetrahedral PO_4

groups delimiting two unconnected channels. The first one has a diameter of 2.5 Å and is bordered by Ca^{2+} ions denoted Ca(I). The second type plays a significant role in the properties of the apatites. It has a diameter of around 3.5 Å and is also delimited by oxygen and Ca^{2+} ions named Ca(II). These channels oriented along the c axis host the $(OH)^-$ groups (or F^- in the case of calcium fluoroapatite) which balance the positive charge of the matrix [19,20]. The apatite structure is very flexible. It accepts various substitutions and ions exchanges in its framework [21,22]. These remarkable properties confer to the material several applications in biotechnology, optics, high temperature fuel cells and catalysis. El Kabouss et al. have studied the calcium-hydroxyapatite (CaHAp) exchanged with cobalt in oxidative dehydrogenation of ethane [10]. Cheikhi et al. showed that MIBK synthesis in one step proceeds effectively on palladium loaded hydroxyapatite. They confirmed that the alkalinity of the support is an important factor in the reaction [23]. Particular interest was also given to the usage of phosphates as supports in methane reforming. The nickel–calcium- phosphate dispersed on hydroxyapatite exhibits reasonable activity and selectivity in partial oxidation of methane [24]. Different species of nickel consisting of supported NiO and Ni^{2+} ions substituting Ca^{2+} in the phosphate were found on the catalyst. It was also shown that Ni–Sr/phosphate is active in partial oxidation of methane [25].

The present work is essentially devoted to the determination of the catalytic performance of the nickel loaded calcium- hydroxyapatite (Ni/CaHAp) and nickel loaded calcium- fluoroapatite (Ni/CaFAp) in carbon dioxide reforming of methane. The carriers were synthesized and impregnated with Ni then characterised by several techniques including electro- nic microscopy, XPS, UV–visible–NIR and temperature programmed reduction (TPR). Special attention was devoted to the determination of correlations between the catalysts activity and the nickel distribution on the different sites of the carrier.

2. Experimental

2.1. Preparation of the supports and the catalysts

Calcium-hydroxyapatite (CaHAp) and calcium-fluoroapatite (CaFAp) were synthesized adding drop wise a boiled aqueous solution of calcium nitrate (1 mol L^{-1}) to a solution of $(NH_4)_2HPO_4$ (0.6 mol L^{-1}) (which in the

case of CaFAp contained also an excess of NH$_4$F) [10,26]. The precipitate was redissolved in a nitric acid solution (2 mol L^{-1}) then neutralised while stirring with ammonia at a pH 9. After filtration, the recovered product was washed well with boiling purified water then dried at 120 °C.

The Ni(x)/CaHAp and Ni(x)/CaFAp were prepared by impregnating at room temperature a given mass of the phosphate with 20 mL of nickel acetate aqueous solutions containing different amounts of Ni. The resulting mixtures were heated with reflux for 1 h and then dried. The recovered residues were calcined at 500 °C in air for 12 h. The samples were named Ni(x)/CaHAp and Ni(x)/CaFAp, where x indicates the weight percentage of Ni. The prepared catalysts contain loads varying from 1 to 10 wt% in nickel.

2.2. Characterization techniques

X-ray diffraction patterns were obtained with a Siemens D5000 high-resolution diffractometer using Ni-filtered Cu Ka radiation. The data were collected at room temperature with a 0.028 step size in 2θ, from 2 θ = 20° to 60°. Crystalline phases were identified by comparison with ICSD reference files.

The textural features and BET surface areas of the samples were determined by equilibrium adsorption and desorption isotherms of N$_2$ at 77 K with a Coulter Omnisorp 100 CX apparatus. The specific surface areas were calculated by applying the BET equation.

Direct observation of the catalysts morphology was carried out by energy-dispersive X-ray spectroscopy (EDS) using a scanning electron microscope JEOL JSM-35C equipped with a NORAN-VOYAGER spectrometer. The shape and the average size of the selected particles were estimated.

FTIR transmission spectra were recorded between 400 and 4000 cm^{-1} at room temperature on a Perkin-Elmer 1600 spectrometer using self-supporting disks of the samples diluted in KBr. This technique is sensitive to the presence of carbonates and pyrophosphates in the samples. It can therefore be used to provide information about their purity.

X-ray photoelectron spectra were recorded on a VG Scientific ESCALAB 200A spectrometer utilizing a non-monochromatized Mg Ka radiation (1253.6 eV). The spectra were digitized, summed, smoothed and reconstructed

using Gauss–Lorentzian components. In order to minimize charge effects, the measurements were carried out on thin pellets placed on an indium plaque. The carbon C 1s peak at 284.6 eV was used as reference.

Diffuse reflectance spectra were recorded at room temperature between 190 and 2500 nm on a Varian Cary 5E spectrometer equipped with a double monochromator and an integrating sphere coated with polytetrafluoroethylene (PTFE). PTFE was also used as a reference.

Thermogravimetric analyses were performed in order to determine the amount of carbon accumulated on the catalysts after the catalytic runs. The equipment used was a Mettler TA 4000 thermal analyser that includes a TG50 thermobalance and TC11 data acquisition system. The experiments were performed using 10-15 mg of the catalyst and an air flow rate of 200 cm^3 min^{-1}.

Temperature programmed reduction (TPR) profiles were recorded at atmospheric pressure using a microreactor containing around 100 mg of oxidized catalyst. This technique was chosen to study the Ni loaded CaHAp and CaFAp, because It can provide information on the location of nickel and its interactions with the carrier. The reduction of the samples was performed with a mixture of H_2/He = 2.5/60 at total flow rate equal to 62.5 cm^3 min^{-1} and a heating rate of 10 °C/min. The hydrogen consumption was measured with a mass spectrometer.

2.3. Catalytic tests

The methane reforming reaction was studied in a quartz fixed bed continuous-flow microreactor operated at atmospheric pressure. Prior to the reaction the catalyst was crushed and sieved to a grain size ranging from 125 to 180 μm. The catalyst (100 mg) was maintained in the reactor between two quartz wool plugs and its temperature measured by a thermocouple placed between the particles of the catalyst. The runs were carried out at 600 °C using a feed mixture composed of CH_4/CO_2/He = 2/2/60 and a total flow rate equal to 64 cm^3 min^{-1}. The reaction products were analysed by mass spectrometry using a SPECTRAMASS Dataquad quadrupole mass spectrometer which was calibrated using different mixtures of CH_4, CO_2, CO and H_2. Before the reaction the catalyst was reduced in situ with a mixture of H_2/ He = 2.5/60 at a total flow rate of 62.5 cm^3 min^{-1} [27]. The reduction temperature was linearly raised from the ambient up to 800 °C using a heating rate of 10 °C/min.

Beside the tests carried out at 600 °C, the catalytic activity of the samples was also measured versus the reaction temperature. In these experiments, no pre-reduction was performed on the catalysts. The temperature of reaction was increased from room temperature up to 800 °C with a heating rate of 5 °C min^{-1}.

The determination of methane and carbon dioxide conversions and hydrogen and carbon monoxide yields were calculated as follows:

$$CH_4 \text{ conversion } (\%) = \frac{(CH_4)_{in} - (CH_4)_{out}}{(CH_4)_{in}} \times 100$$

$$CO_2 \text{ conversion } (\%) = \frac{(CO_2)_{in} - (CO_2)_{out}}{(CO_2)_{in}} \times 100$$

$$H_2 \text{ yield } (\%) = \frac{(H_2)_{out}}{(CH_4)_{in}} \times \frac{100}{2}$$

$$CO \text{ yield } (\%) = \frac{(CO)_{out}}{(CH_4)_{in} + (CO_2)_{in}} \times 100$$

The margin of error is around 1.2-1.5%.

3. Results and discussion

3.1. Catalysts characterization

3.1.1. Adsorption isotherms and specific surface areas

N_2 adsorption at 77 K on CaHAp and CaFAp showed that the isotherms display in the P/P_0 range of 0.2–0.4 an inflection which is characteristic of mesoporous solids of type IV according to the IUPAC classification. At the ratio $P/P_0 = 0.98$, the volume of nitrogen adsorbed on the hydroxyapatite reached 0.316 cm^3/g, while it was only about 0.270 cm^3/g on the fluoroapatite. This result is in agreement with the analysis performed by mercury porosimetry which showed that the fluoroapatite is denser than the hydroxyapatite (Table 1). Loading both carriers with Ni up to 10% does not modify the shape of the adsorption isotherms. The nitrogen desorption gives rise to a hysteresis loop, which is often observed when the aggregated particles form a heterogeneous

assembly of capillaries with various sized entrances [28].

Table 1 reports specific surface areas of the samples calcined at 500 °C for 12 h. The hydroxyapatite has a specific surface area slightly larger than that of the fluoroapatite. Addition of nickel to CaHAp and CaFAp does not seem to notably modify their specific surface areas.

3.1.2. Scanning electron microscopy

Ni loaded and unloaded phosphates were investigated by scanning electron microscopy in order to visualise the textural modifications introduced by addition of nickel on both carriers. The micrographs of the CaHAP and CaFAP calcined at 500 ºC (Fig. 1a and d) show no difference in the aspect of the two carriers, except that the particles of CaHAP are of about twice the size (40 nm) of those of CaFAP (20 nm). In both cases a spherical shape is observed.

The analysis of the impregnated samples indicates that addition of nickel increases the size of the catalyst particles. In the case of Ni(x)/CaHAp, the particle size goes from 45 to 60 nm when the Ni load goes from 4 to 8% (Fig. 1b and c). For Ni(x)/CaFAp a similar change occurs from 90 to 120 nm for the same modification of Ni loadings (Fig. 1e and f). The morphology of the particles is also affected by the addition of nickel. Ni(x)/CaFAp exhibit a variety of forms, while the shape of Ni(x)/CaHAp particles remains spherical as in case of pure hydroxyapatite. Microanalysis (EDS) of the catalysts showed that the nickel is homogeneously dispersed on the particles examined. Its distribution appears to be quite similar on both series of catalysts, despite the morphological differences observed between them.

3.1.3. X-ray diffraction (XRD)

X-ray diffraction patterns of CaHAp and CaFAp were found to be identical to the reference patterns reported in the literature (JCPDS 9432, JCPDS 0876) confirming that the synthesized phosphates are pure apatites (Fig. 2a and d). The diffractograms of Ni(x)/CaHAP and Ni(x)/CaFAp show no lines of NiO for loads of 4 wt% and below. Above this concentration two typical peaks belonging to NiO appear at $2\theta = 37.6°$ and 42.6° (Fig. 2b and e). Their

intensity increases with nickel loading.

X-ray diffraction patterns of Ni(x)/CaHAp and Ni(x)/CaFAp after the reduction at 800 °C are presented on Fig. 2c and f which show that the NiO is completely reduced into metallic Ni (peak at 44.6°) without modifying the phosphate structure.

3.1.4. FTIR spectroscopy

The infrared spectra of CaHAp and CaFAp are analogous to those described in the literature for apatite-type structures (Fig. 3a and d). Calcium-hydroxyapatite is characterized by two bands appearing at 3775–3530 and 750–620 cm^{-1}, ascribable to the symmetrical valence vibrations (v_s) and to the vibrational oscillations (v_L)of the hydroxyls, respectively [29]. These bands do not exist in the spectrum of the fluoroapatite since the hydroxyls were substituted by F$^-$ ions in the network. In the range 400–1200 cm^{-1} all the spectra display three bands located at 965, 1035 and 1094 cm^{-1} characteristic of the vibration modes of P–O bonds in $(PO_4)^{3-}$ groups [30]. The absence from the spectra of the band around 875 cm^{-1} usually assigned to HPO_4^{2-} anions indicates that further heating of the samples above 500 °C will not yield pyropho- sphates according to the condensation process $2HPO_4^{2-} \longrightarrow P_2O_7^{4-}$. In the domain 1300–1600 cm^{-1}, there are bands at 1394.7 and 1456.7 cm^{-1} which are due to the presence of carbonates $(CO_3)^{2-}$ in the samples and probably also to adsorbed CO_2 [30].

Addition of nickel to CaHAp decreases the intensity of the band assigned to the hydroxyl groups but does not affect significantly the rest of the spectra (Fig. 3b and c). Reduction of the samples at 800 °C (H$_2$/He = 2.5/60) does not modify the vibrational modes of the different bonds in Ni(x)/CaHAp and Ni(x)/CaFAp.

3.1.5. UV–visible–NIR (DRS)

Diffuse reflectance spectroscopy was used to study the symmetry and the coordination of nickel species dispersed on CaHAp and CaFAp. The Ni^{2+} (3d^8) ions in octahedral surrounding exhibit a simple spectrum (^{3}F fundamental term and ^{3}P excited term) that involves three spin allowed d–d transitions appearing

in the near infrared (NIR) and in the visible domain. Moreover, there is no Jahn Teller effect. These transitions are usually located around 930–1660 nm for the ν_1 ($^3A_{2g} \longrightarrow {}^3T_{2g}$) transition, 570–1000 nm for n_2 ($^3A_{2g} \longrightarrow {}^3T_{1g}$) transition and 360–520 nm for n_3 ($^3A_{2g} \longrightarrow {}^3T_{1g}$ (P)) transition. The values of the crystal field parameters are generally small resulting in d–d transition bands displaying low intensities.

Fig. 4a–c show the spectra of Ni(x)/CaHAp. They display several bands located in the NIR region at 1385, 1425, 1930 and 2220 nm [10,23]. These bands are all attributed to the vibration modes of OH groups. The narrow one centred at 1425 nm was assigned to the free OH$^-$ hydroxyls located in the tunnels of the apatite. In the UV-visible region, the spectra show also bands around 210, 285, 420 and 730 nm. The band centred at 210 nm was attributed to $O^{2-} \longrightarrow Ca^{2+}$ charge transfers. When the amount of Ni loaded exceeds 4 wt%, this band is overlapped by a second one associated with $O^{2-} \longrightarrow Ni^{2+}$ charge transfers, which appears at 285 nm and increases with the Ni concentration in the samples. In the visible domain, the bands located at 420 and 730 nm are due to the n_3 and n_2 transitions of Ni^{2+} ions in an octahedral or pseudo-octahedral symmetry [31,32]. The broad band appearing in the NIR around 1210 nm, for nickel loadings around 1 wt% is attributed to n_1 transition. The increase of Ni concentration enhances the broadening of the band indicating that there is formation of NiO on the surface of the phosphate. Therefore, it might be concluded that at low loadings ($x < 1$ wt%) nickel is exchanged with Ca^{2+} ions of the apatite framework, and at loadings superior to 1 wt% it stays as NiO on the surface of the carrier.

Fig. 4d–f present UV–visible–NIR spectra of Ni(x)/CaFAp. The absorption band centred at 420 nm and previously attributed to ν_3 transitions of Ni^{2+} is now better resolved. All the transition bands due to Ni^{2+} ions in octahedral symmetry are also present in the spectra. For low Ni contents ($x \leq 1$ wt%), the spectra were attributed to the Ni^{2+} ions exchanged with the Ca^{2+} ions located in the pseudo-octahedral sites of the apatite framework as in the case of Ni(x)/CaHAp. For loadings higher than 1 wt% Ni, the shapes of the Ni(x)/CaFAp spectra change markedly, because particles of NiO start to appear on the surface of the support. Obviously, the two species coexist at high contents and the bands of NiO overlap those attributed to Ni^{2+}/Ca^{2+} exchanged ions. A comparison of the UV–visible spectra of the Ni(x)/CaHAp before and after the reduction of the samples

confirmed that the reduction of NiO into metallic Ni is complete. The bands located at 420 and 730 nm (due to NiO), have practically disappeared. Similar observations were made in the case of Ni(x)/CaFAp, confirming that the NiO reduction proceeds on both samples via analogous pathways.

3.1.6. X-ray photoelectron spectroscopy (XPS)

Several studies of oxidized and reduced forms of supported and unsupported nickel were performed by XPS and reported in the literature [33,34]. The aim of the present work is to identify the chemical state of the nickel laying on the surface of the two phosphates. The XPS spectra in the Ni $2p_{3/2}$ region of Ni(x)/ CaHAp, for various nickel loadings contain three peaks appearing around the binding energies 854.4, 856.0 and 857.0 eV suggesting that Ni is at least distributed between three different sites (Fig. 5). The shape of Ni(x)/CaFAp and Ni(x)/ CaHAp XPS spectra are almost identical. The peak located at 854.4 ± 0.3 eV which appears on Ni(x)/CaHAp as well as on Ni(x)/CaFAp is attributed to the binding energy of Ni $2p_{3/2}$ in NiO dispersed on the phosphate [35,36]. The second peak centred on 855.7 ± 0.3 eV was also ascribed to Ni $2p_{3/2}$ in NiO particles interacting more strongly with the carrier. The peak located between 856 and 857 eV was observed by Dissanyake et al. in the spectra of Ni(OH)$_2$, NiAl$_2$O$_3$, NiSO$_4$ and NiSiO$_3$ and it was assigned to Ni^{2+} ions in the network of these compounds [37,38]. On the other hand, Lee et al. observed analogous peaks with nickel–calcium-phosphate supported on hydroxyapatite catalysts and ascribed them to two types of Ni^{2+} ions involved in two different environments (PO–Ni–OP) and (HO–Ni–OP) [25]. Therefore, the third peak which appears at 856.9 ± 0.3 eV might be associated with Ni^{2+}/Ca^{2+} ion exchange that was performed in the two sites Ca(I) and Ca(II) of the apatite during the impregnation process. The samples do not show any peak at 852.0 eV because they were exposed to oxidizing atmosphere and do not contain metallic nickel. The spectra of Ni(x)/CaHAp and Ni(x)/CaFAp also exhibit typical shake-up satellite peak close to 861.4 ± 0.3 eV [37].

Table 2 summarises the results and shows that the distribution of Ni^{2+} ions between the different sites that were previously detected in the samples depends on the nature of the support. On Ni(x)/CaHAp, the percentage of exchanged Ni^{2+}/Ca^{2+} ions decreases from 61 to 34.5%, while passing from 1 to 2 wt% of loaded Ni. The amount

of supported NiO increases with the nickel content but stays almost constant after 1 wt%. In the case of Ni(x)/CaFAp, the distribution of Ni between the three sites does not seem to depend on Ni content, suggesting that the amount of Ni^{2+} exchanged in CaFAp is quite lower than in CaHAp.

3.1.7. Temperature programmed reduction (TPR)

Fig. 6 displays the TPR profiles of Ni(x)/CaHAp for different Ni loadings. The spectrum of Ni(1)/CaHAp shows three distinct peaks centred on 500, 630 and 720 °C (Fig. 6a). The first one was assigned to the reduction of small particles of NiO which have strong interaction with the support [24,39]. The two following peaks located at higher temperatures were attributed to the reduction of two types of Ni^{2+} ions incorporated in the Ca(I) and Ca(II) sites of CaHAp. Moreover, the hydrogen uptake above 550 °C does not change signifi- cantly when the nickel content is increased suggesting that the amount of exchanged nickel is about 1 wt%. Similar high reduction temperatures of nickel were observed with Ni/Al$_2$O$_3$ [40]. Hydrogen consumption gives rise, depending on the alumina properties, to two peaks between 500 and 800 °C. The first one is usually ascribed to the reduction of the NiO strongly interacting with the carrier and the second to the reduction of NiAl$_2$O$_4$ phase that appears in the catalyst. Therefore, on Ni(1)/ CaHAp a large fraction of the loaded nickel is exchanged with Ca^{2+} ions of the hydroxyapatite structure, the rest is spread as NiO over the carrier [24].

The spectrum of the Ni(2)/CaHAp (Fig. 6b) shows a first peak at 420 °C which was not observed in the case of Ni(1)/ CaHAp (Fig. 6a). It was attributed to NiO that is more easily reducible than the one associated with the peak at 500 °C [41,42]. The spectrum exhibits also two peaks located above 550 °C which were assigned to the reduction of the Ni^{2+} ions incorporated in the apatite. For nickel loadings superior to 2 wt%, the hydrogen consumption starts around 250 °C (Fig. 6c–e). The maximum of the first reduction peak shifts, as expected, slightly toward low temperatures as the Ni loading is increased. The intensity of the peak also progressively increases with the addition of nickel. For high Ni contents (x = 10%) the peak overlaps all the others probably because the size of free NiO particles increases and their reduction process becomes the prevalent phenomenon [24].

12

Fig. 7 reports TPR profiles of Ni(x)/CaFAp, for different nickel loadings. It shows that the amount and the location of the peaks differ from that of Ni(x)/CaHAp. For $x = 1$ and 10%, it displays only two broad peaks (Fig. 7a and e), while for $x = 2$, 4 and 8% it shows three peaks (Fig. 7b–d). Moreover, there is none above 700 ºC. On Ni(1)/CaFAp, the two H_2 up takes are centred on 460 and 575 ºC (Fig. 7a); while, in the case of Ni(2)/CaFAp they appear at 410, 500 and 580 ºC (Fig. 7b). Globally, the increase of Ni loading shifts the peaks toward lower temperatures except for $x = 10$%. As in the case of Ni(x)/CaHAp, the H_2 consumptions below 550 ºC were ascribed to reduction of free NiO particles and to those strongly interacting with the phosphate. Above 550 ºC, whatever the loading is, there is only one peak that was due to the reduction of Ni^{2+} ions incorporated in the phosphate, instead of two in the case of Ni(x)/CaHAp. A recent study of cation substitutions in apatites reported that in fluoroapatite systems a preferential occupation of one of the two sites Ca(I) or Ca(II) might occur [43]. The nickel in Ni(x)/ CaFAp probably occupy only the sites Ca(II) which in the structure seem to be more accessible. This result confirms that TPR is a powerful tool, which can provide more valuable information than the typical sophisticated techniques. In the case of Ni(x)/CaHAp and Ni(x)/CaFAp it allowed us to easily distinguish the different species of Ni^{2+} ions and the quantitative features of the carriers. The revealed differences between Ni(x)/CaHAp and Ni(x)/CaFAp might influence and explain the catalytic behaviour of those systems.

3.2. Dry reforming of methane over Ni(x)/CaHAp and Ni(x)/CaFAp

Table 3 shows CH_4 and CO_2 conversions and CO and H_2 yields, at 600 ºC and stationary state. Over Ni(4)/CaHAp, Ni(8)/CaHAp and Ni(10)/CaHAp, the methane and CO_2 conversions as well as CO and H_2 yields are stable from the start of the reaction. The best methane conversion (78%), H_2 (56%) and CO (81%) yields were achieved with Ni(4)/CaHAp. For nickel loadings inferior to 2 wt%, the catalysts demonstrated the poorest performance. The activity does not exceed 10% (Table 3).
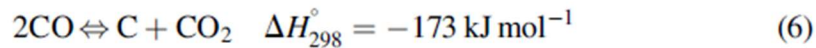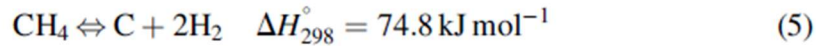
The conversions of CH_4 and CO_2 and the yields of H_2 and CO obtained with Ni(x)/CaFAp are similar to those achieved with Ni(x)/CaHAp (Table 3). The activity of the catalysts containing nickel loadings $x > 2$ wt% increases slightly at the start of the reaction, probably because of an activation of the catalysts. After 50 min, this transitory

state reaches a stable and rather significant conversion of CH_4 and CO_2, producing large quantities of H_2 and high CO selectivity. The increase of nickel loading increases the H_2 yield, which attains 59% for the catalysts containing 8–10 wt% of Ni. Carbon monoxide production also increases up to 82% when using Ni(10)/ CaFAp. The progressive addition of nickel improves CO_2 conversion. Moreover, CO_2 conversion (Table 3) is always greater than that of CH_4 because the production of synthesis gas from CH_4 and CO_2 (2) is probably influenced by the occurrence of the reverse water-gas shift reaction (4). The H_2/CO ratio is in all the cases lower than 1:

$$CO_2 + H_2 \Leftrightarrow CO + H_2O \quad \Delta H^{\circ}_{298} = 41 \, \text{kJ mol}^{-1} \qquad (4)$$
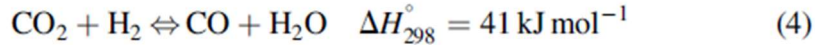
The conversions achieved at high nickel loadings ($x > 2$) are all close to the thermodynamic equilibrium which for overall reactions and the chosen conditions, is around 78%.

Table 3 shows also the amounts of carbon deposited on the catalysts after 4 h of reaction. The increase of nickel loading on both series increases carbon deposition which occurs mainly by methane cracking (5) and CO disproportionation (6). However, the reverse reaction of (6) might also contribute to the increase of CO yields and to the understanding of the low amount of carbon deposited on the catalysts [44,45]:

$$CH_4 \Leftrightarrow C + 2H_2 \quad \Delta H^{\circ}_{298} = 74.8 \, \text{kJ mol}^{-1} \qquad (5)$$

$$2CO \Leftrightarrow C + CO_2 \quad \Delta H^{\circ}_{298} = -173 \, \text{kJ mol}^{-1} \qquad (6)$$

It is also worthy to notice that the calcium-apatites have basic properties. They can reversibly adsorb carbon dioxide giving rise at least to two types of carbonate apatites [17]. Although, the mechanism of this CO_2 incorporation in the phosphate is complex, it enhances the chemical reactivity and basic character of the apatites. It was also observed that strong Lewis basicity inhibits carbon deposition on the active sites by shifting the equilibrium concentrations of CO disproportionation [46]. Furthermore, the literature has reported that the basicity has a positive effect on the performance of the catalysts in methane reforming [47]. It is probably these basic features that make of the apatite such interesting carrier. For instance, at 600 °C Ni/Mg-Al$_2$O$_3$ has in methane reforming a conversion of 61%; whereas, over our catalysts it exceeds 75% [48].

Methane is also known to chemisorb dissociatively on several transition metals giving rise to an evolution of hydrogen and adsorbed CH_x species which by recombination produce large fragments C_mH_n on the catalyst. The

hydrogenolysis of these carbonaceous species was shown to generate higher hydrocarbons [49]. If not hydrogenolysed these species can act as a poison to the active sites. In the presence of oxygen generated by the dissociation of CO_2 these C_mH_n fragments might be oxidized and evacuated [50–53].

Fig. 8 shows the variations of methane conversion over Ni(x)/CaHAp and Ni(x)/CaFAp versus the reaction temperature which was linearly increased up to 800 ºC. The experiments were carried out using fresh catalysts. Only the results obtained with Ni(4)/CaHAp and Ni(4)/CaFAp were reported here because they are the most significant. On Ni(4)/CaHAp methane activation starts around 500 ºC. Its conversion increases rapidly to reach about 98% at 650 ºC, then it stays constant up to 800 ºC. On Ni(4)/CaFAp methane conversion begins at approximately 450 ºC but it does not reach 98% before 800 ºC. A second catalytic run, performed on the same catalysts revealed a decrease of the temperature of methane activation. The methane conversion starts around 350 ºC and increases less abruptly than in the first increase. Moreover, the temperature corresponding to 50% of methane conversion (Table 4) is also lower than on the fresh catalysts, probably because the reaction mixture reduces NiO quite rapidly to metallic nickel. This is in agreement with the UV–visible spectra of the catalysts recorded before and after the runs which confirm that the bands of NiO have disappeared.

Fig. 9 shows CO_2 conversion versus the temperature on Ni(4)/CaHAp and Ni(4)/CaFAp. All the conclusions previously drawn for methane reforming remain appropriate. In the case of Ni(4)/CaHAp, the temperature at which CO_2 conversion reaches 50% is lower by at least by 20 ºC from the first to second catalytic run (Table 4). Moreover, CO_2 conversion on Ni(4)/CaHAp reaches only 84% at 800 ºC, while on Ni(4)/ CaFAp it attains 99% at the same temperature. This difference in the catalytic behaviour of the two catalysts is probably due to the nature of Ni interactions with the carriers.

Fig. 10 displays H_2 yields versus the reaction temperature. The shape of the curves is similar to that of methane conversion. The hydrogen yield is of about 90% at 800 ºC and the CO/H_2 is lower than 1. All the results are in agreement with the previous ones performed at constant temperature and indicate that the conversions are at thermodynamic equilibrium.

FTIR spectroscopy, UV–visible spectra and XRD patterns of the catalysts recorded after the tests did not show any

noticeable difference with that of the reduced samples suggesting that they did not undergo any noticeable alteration during the reaction.

4. Conclusions

The Ni(x)/CaHAp and Ni(x)/CaFAp catalysts were prepared and characterized by DRX, IR, UV–visible–PIR, XPS and TPR. UV–visible spectroscopy showed that both series of catalysts contain supported NiO for Ni loads of 2 wt% and above, whereas at low nickel contents the Ni^{2+} ions are exchanged with Ca^{2+} ions of the apatite. TPR and XPS analyses confirmed that Ni exists in three forms in the samples: (i) large crystallites of NiO deposited on the surface of catalysts, (ii) NiO in small particles exhibiting strong interaction with the support and (iii) a phase where nickel is partially exchanged with calcium ions in the structure of the phosphate. Moreover, the distribution of the loaded nickel between these different forms as shown by XPS depends on the nature of the carrier. Carbon dioxide reforming of methane over Ni(x)/CaHAp and Ni(x)/CaFAp at 600 ºC showed that the conversions at all temperatures are managed by the thermodynamic equilibrium and the H_2/CO ratio lower than 1. Similar catalytic results were obtained when the tests are performed in non-isothermal conditions.

References

[1]   A.T. Ascroft, A.K. Cheetman, M.L. Green, P.D.F. Vernon, Nature 352 (1991) 225.
[2]   K. Nagaoka, K. Seshan, K. Aika, J.A. Lercher, J. Catal. 197 (2001) 34.
[3]   E. Ruckenstein, H.Y. Wang, J. Catal. 205 (2) (2002) 289.
[4]   J. Wei, E. Iglesia, J. Catal. 225 (2004) 116.
[5]   A.M. O'Connor, J.R.H. Ross, Catal. Today 46 (1998) 203.
[6]   M.A. Ermakova, D.Yu. Ermakov, G. Kuvshinov, Appl. Catal. A: Gen. 201 (2000) 61.
[7]   K. Takehira, T. Shishido, P. Wang, T. Kosaka, Ken Takaki, J. Catal. 221 (2004) 43.
[8]   M.C.J. Bradford, M.A. Vannice, Appl. Catal. A 142 (1996) 73.
[9]   V.R. Choudhary, A.S. Mamman, Appl. Energy 66 (2000) 161.

[10] K. Elkabouss, M. Kacimi, S. Amar, F. Bozon-Verduraz, M. Ziyad, J. Catal. 226 (2004) 16.

[11] J. El-Edrissi, M. Kacimi, M. Loukah, M. Ziyad, J. Chim. Phys. 94 (1997) 1984.

[12] J.R. Rostrup-Nielsen, in: J.R. Anderson, M. Boudart (Eds.), Catalysis, Science and Technology, vol. 5, Springer, Berlin, 1999, p. 1.

[13] M.C.J. Bradford, M.A. Vannice, Catal. Rev. Sci. Eng. 41 (1999) 1.

[14] C.T. Au, H.Y. Wang, J. Catal. 167 (1997) 337.

[15] J.R. Rostrup-Nielsen, J.H.B. Hansen, J. Catal. 144 (1993) 38.

[16] (a) P.D.F. Vernon, M.L.H. Green, A.K. Cheetam, A.T. Ashcroft, Catal. Today 13 (1992);

(b) P.D.F. Vernon, M.L.H. Green, A.K. Cheetam, A.T. Ashcroft, Materials 3 (2002) 271.

[17] J.C. Elliot, Structure and Chemistry of the Apatites and Other Calcium Orthophosphates, Elsevier, Amsterdam, 1994.

[18] K. Sudarsanan, P.E. Mackie, R.A. Young, Mater. Res. Bull. 7 (1972) 1331.

[19] J.C. Rendon-Angeles, K. Yanakisawa, N. Ishizawa, S. Oishi, J. Solid State Chem. 151 (2000) 65.

[20] J.C. Rendon-Angeles, K. Yanakisawa, N. Ishizawa, S. Oishi, Chem. Mater. 12 (2000) 2143.

[21] M.E. Fleet, Y. Pan, J. Solid state Chem. 111 (1994) 78.

[22] M.E. Fleet, Y. Pan, Am. Miner. 82 (1997) 870.

[23] N. Cheikhi, M. Kacimi, M. Rouimi, M. Ziyad, L.F. Liotta, G. Pantaleo, G. Deganello, J. Catal. 232 (2005) 257.

[24] J.H. Jun, T. Lee, T.H. Lim, S. Nam, S. Hong, K.J. Yoon, J. Catal. 221 (2004) 178.

[25] S.J. Lee, J.H. Jun, S. Lee, K.J. Yoon, T.H. Lim, S. Nam, S. Hong, Appl. Catal. A: Gen. 230 (2002) 61.

[26] Z. Boukha, M. Kacimi, F. Bozon-Verduraz, M. Ziyad, in: Proceedings of the 13th International Congress on Catalysis, Paris, France, July 11–16, 2004.

[27] Y.G. Chen, K. Tomishige, K. Yokoyama, K. Fujimoto, J. Catal. 184 (1999) 479.

[28] K.S.W. Sing, D.H. Everett, R.A.W. Haul, L. Moscou, R.A. Pierotti, J. Rouque´rol, T. Siemieniewska, Pure Appl. Chem. 57 (1985) 603.

[29] H. Widjaja, K. Eguchi, Bull. Chem. Soc. Jpn. 72 (1999) 313.

[30] K. Yamashita, H. Owada, T. Kanazawa, T. Umekaki, Solid State Ionics 28–30 (1988) 660.

[31] J. Abart, E. Delgado, G. Ertl, H. Jeziorowski, H. Knozinger, N. Thiele, X.Z. Wang, App. Catal. 2 (1982) 155.

[32] A.B.P. Lever, Inorganic Electronic Spectroscopy, 2nd ed. Studies in Physical Theorical Chemistry, vol. 33, Amsterdam, Elsevier, 1984, p. 481.

[33] R. Molina, G. Poncelet, J. Phys. Chem. B 103 (1999) 11290.

[34] C.P. Li, A. Proctor, D.M. Hercules, Appl. Spectrosc. 38 (1984) 880.

[35] C.D. Wagner, W.M. Riggs, L.E. Davis, J.F. Moulder, G.E. Muilenberg, Handbook of X-ray Photoelectron Spectroscopy, Perkin Elmer, Eden Prairie, USA, 1979.

[36] M. Lenglet, F. Hochu, J. Durr, M.H. Tuilier, Solid State Commun. 104 (1997) 793.

[37] D. Dissanyake, M.P. Rosynek, J.H. Lunsford, J. Phys. Chem. 97 (1993) 3644.

[38] D. Briggs, M.P. Seach (Eds.), 2nd ed., Pratical Surface Analysis: Auge Rand X-ray Photoelectron Spectroscopy, vol. 1, Wiley, New York, 1990, App 5.

[39] E. Asedegbega-Nieto, B. Bachiller-Baeza, A. Guerrero-Ruy´´z, I. Rodry´'- guez-Ramos, Appl. Catal. A: Gen. 300 (2006) 120.

[40] C. Guimon, A. Auroux, E. Romero, A. Monzon, Appl. Catal. A 251 (2003) 199.

[41] J. Guo, H. Lou, H. Zhao, D. Chai, X. Zheng, Appl. Catal. A: Gen. 273 (2004) 75.

[42] W. Dong, K.W. Jun, H. Roh, Z.W. Liu, S. Park, Catal. Lett. 78 (2002) 215.

[43] T. Tamm, M. Peld, J. Solid State Chem. 179 (2006) 1580.

[44] K. Tomishige, Y. Himeno, Y. Matsuo, Y. Yoshinaga, K. Fujimoto, Ind. Eng. Chem. Res. 39 (2000) 189.

[45] K. Nagaoka, M. Okamura, K. Aika, Catal. Commun. 2 (2001) 255.

[46] T. Horiuchi, K. Sakuma, T. Fukui, Y. Kubo, T. Osaki, T. Mori, Appl. Catal. A 144 (1996) 111.

[47] J.Y. Mehr, K.J. Jozani, A.N. Pour, Y. Zamai, React. Kinet. Catal. Lett. 75 (2002) 267.

[48] A.I. Tsyanok, K. Takehira, T. Hayakawa, Catal. Lett. 77 (2001) 75.

[49] N. Cheikhi, M. Ziyad, G. Coudurier, J.C. Ve´drine, Appl. Catal. A 118 (1994) 187.

[50] V.C.H. Kroll, H.M. Swaan, S. Lacombe, C.J. Mirodatos, J. Catal. 167 (1997) 387.

[51] S.T. Seyer, Q.Y. Yang, M.B. Lee, A.D. Johnson, Methane Conversion, vol. 51, Elsevier, Amsterdam, 1993.

[52] T. Osaki, H. Masuda, T. Mori, Catal. Lett. 29 (1994) 33.

[53] H.M. Swaan, V.C.H. Kroll, G.A. Martin, C. Mirodatos, Catal. Today 21 (1994) 571.

Sample	Density (g/cm³)	Ni (wt%)	V_{ads} (cm³/g)[a]	S (m²/g)	Ni reduction peak, T (°C)[b]	Ni in the sites (%)
	0.92	0	0.316	55	–	–
		1	0.205	40	500 (2)	06.46
					630 (3)	83.87
					720 (4)	09.67
		2	0.210	43	420 (1)	24.76
					500 (2)	40.48
					630 (3)	30.58
					720 (4)	04.18
		4	0.215	48	395 (1)	32.45
CaHAp and Ni(x)/CaHAp					490 (2)	42.15
					630 (3)	23.75
					730 (4)	03.65
		8	0.205	47	410 (1)	56.56
					505 (2)	31.21
					625 (3)	10.30
					730 (4)	01.93
		10	0.205	50	410 (1)	71.20
					500 (2)	23.60
					610 (3)	05.20
	1.055	0	0.270	45	–	–
		1	0.210	50	455 (2)	66.50
					575 (3)	33.50
		2	0.210	53	410 (1)	46.96
					515 (2)	29.54
					595 (3)	23.50
		4	0.210	53	380 (1)	47.62
CaFAp and Ni(x)/CaFAp					495 (2)	37.43
					580 (3)	14.94
		8	0.215	43	380 (1)	48.80
					460 (2)	46.60
					580 (3)	04.60
		10	0.215	42	400 (1)	78.15
					460 (2)	17.35
					580 (3)	04.50

(1) NiO which has weak interaction with the support. (2) NiO which has strong interaction with the support. (3) Ni^{2+} incorporated in the Ca(II) sites of apatite. (4) Ni^{2+} incorporated in the Ca(I) sites of apatite.

[a] Volume of adsorbed nitrogen at $P/P_0 = 0.98$.

[b] Determined by H_2-TPR.

Table 1. Specific surface areas of the Ni(x)/CaHAp and Ni(x)/CaFAp

Catalysts	Ni (at.%)	Ni/Ca (at.%)	Ni $2p_{3/2}$ (eV)	Ni (%)in the sites
Ni(1)CaHAp	1.06	5.28	856.9 (3)	61.0
			855.7 (2)	29.5
			854.4 (1)	09.5
Ni(2)CaHAp	1.62	7.96	857.0 (3)	34.5
			855.7 (2)	38.0
			854.0 (1)	27.5
Ni(4)CaHAp	2.22	11.12	857.0 (3)	31.4
			855.8 (2)	38.1
			854.1 (1)	30.5
Ni(8)/CaHAp	2.51	12.72	856.7 (3)	30.9
			855.4 (2)	39.3
			853.8 (1)	29.8
Ni(1)CaFAp	1.37	6.2	857.1 (3)	32.9
			855.7 (2)	39.1
			854.1 (1)	28.0
Ni(2)CaFAp	1.73	7.9	857.0 (3)	36.0
			855.6 (2)	36.5
			854.0 (1)	27.5
Ni(4)/CaFAp	2.38	11.60	856.9 (3)	34.4
			855.6 (2)	39.4
			854.0 (1)	26.2
Ni(8)/CaFAp	2.57	12.8	856.8 (3)	38.7
			855.4 (2)	33.9
			853.9 (1)	27.4

(1) NiO which has weak interaction with the support. (2) NiO which has strong interaction with the support. (3) Ni^{2+} incorporated in the Calcium sites of apatite.

Table 2. Results of XPS analysis in the energy range of Ni 2p

Catalusys	Conversion (%)		Yield (%)		H_2/CO	$(g_C/g_{cat}) \times 10^2$
	CH_4	CO_2	CO	H_2		
Ni(1)/CaHAp	22	28	21	5	0.26	0.3
Ni(2)/CaHAp	73	78	74	48	0.72	0.3
Ni(4)/CaHAp	78	78	81	56	0.70	0.5
Ni(8)/CaHAp	75	80	78	54	0.68	0.7
Ni(10)/CaHAp	75	82	77	53	0.73	1.0
Ni(1)/CaFAp	16	20	9.7	2.5	0.29	0.4
Ni(2)/CaFAp	38	47	42	21	0.51	0.4
Ni(4)/CaFAp	75	81	78	53	0.70	0.6
Ni(8)/CaFAp	78	81	80	59	0.77	0.9
Ni(10)/CaFAp	80	83	82	59	0.74	1.1

Table 3. Catalytic activity at the stationary state and 600 ºC of Ni(x)/CaHAp and Ni(x)/ CaFAp in the methane dry reforming with CO_2 (after 4 h on stream)

Catalysts	First increase			Second increase		
	$T_{50}CH_4^{(a)}$	$T_{50}CO_2^{(b)}$	$T_{50}H_2^{(c)}$	$T_{50}CH_4^{(a)}$	$T_{50}CO_2^{(b)}$	$T_{50}H_2^{(c)}$
Ni(4)/CaHAp	555	538	555	487	515	542
Ni(4)/CaFAp	517	515	492	513	515	512

(a) Defined as the temperature required for 50% methane conversion. (b) Defined as the temperature required for 50% CO_2 conversion. (c) Defined as the temperature required for 50% H_2 yield.

Table 4. Catalytic activity vs. the reaction temperature over Ni(4)/CaHAp and Ni(4)/CaHAp
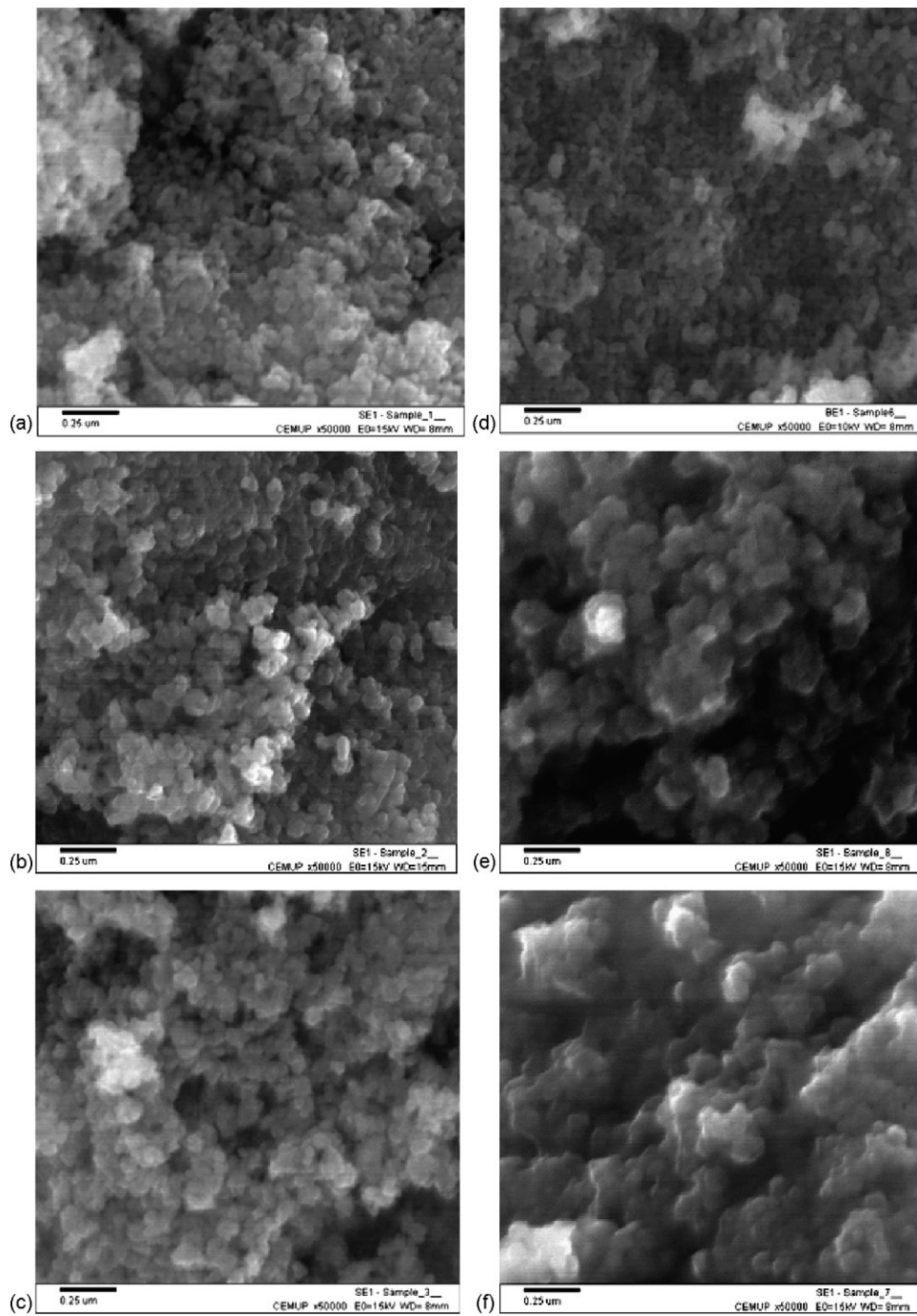
Fig. 1. SEM images of (a) CaHAp; (b) Ni(4)/CaHAp; (c) Ni(8)/CaHAp; (d) CaFAp; (e) Ni(4)/CaFAp; (f) Ni(8)/CaFAp.
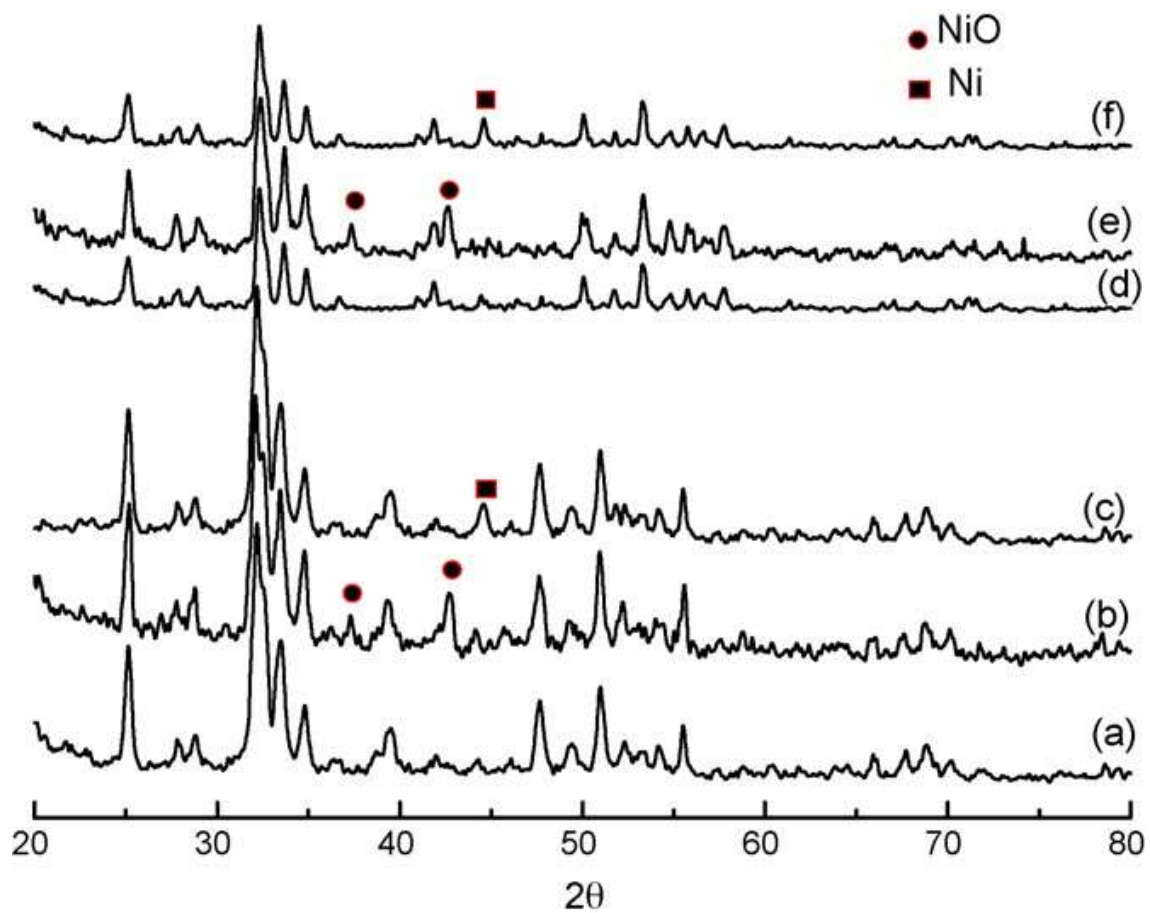
Fig. 2. XRD patterns of (a) CaHAp; (b) Ni(10)/CaHAp; (c) Ni(10)/CaHAp after the reduction of the sample at 800 ºC; (d) CaFAp; (e) Ni(10)/CaFAp; (f) Ni(10)/CaFAp after the reduction of the sample at 800 ºC.
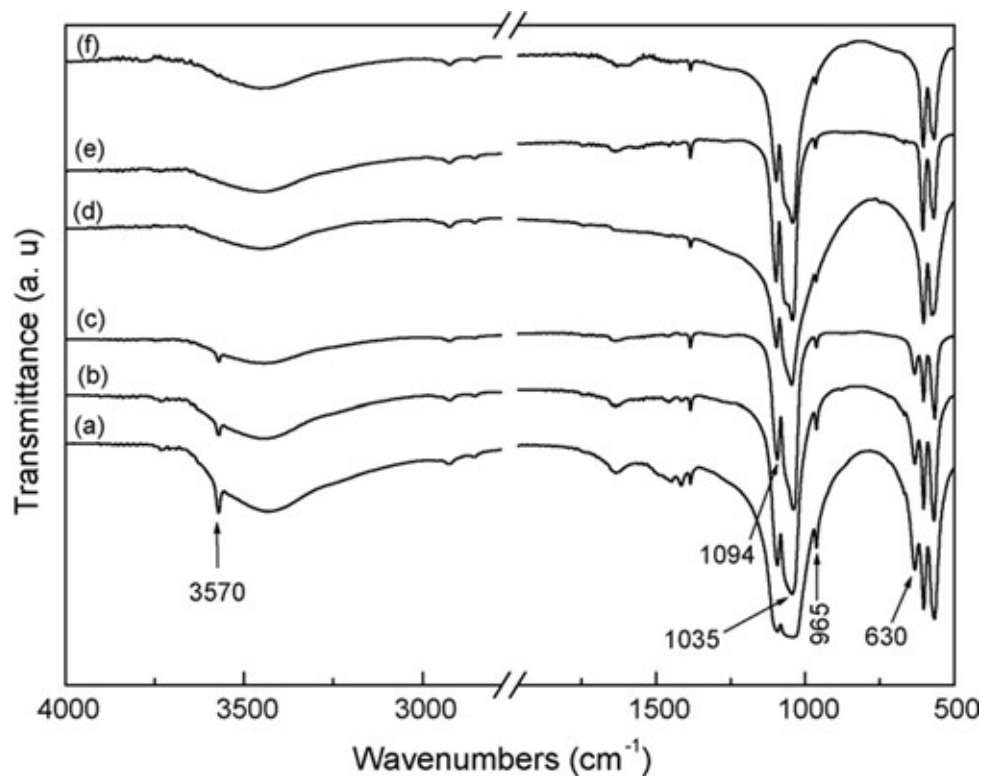
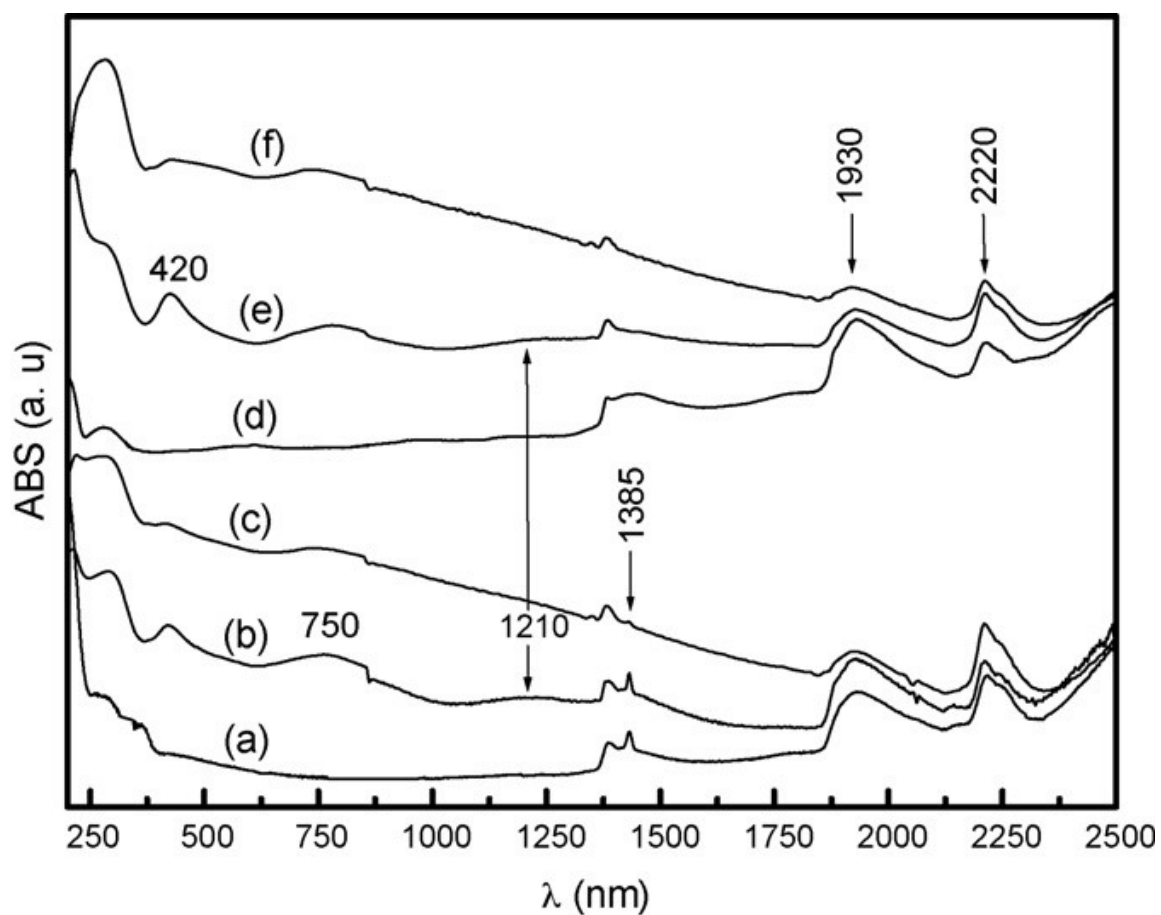Fig. 3. IR spectra of (a) CaHAp; (b) Ni(4)/CaHAp; (c) Ni(8)/CaHAp; (d) CaFAp; (e) Ni(4)/CaFAp; (f) Ni(8)/CaFAp.

Fig. 4. UV–VIS–NIR spectra of (a) CaHAp; (b) Ni(1)/CaHAp; (c) Ni(4)/ CaHAp; (d) CaFAp; (e) Ni(1)/CaFAp; (f) Ni(4)/CaFAp calcined at 500 ºC, under air.
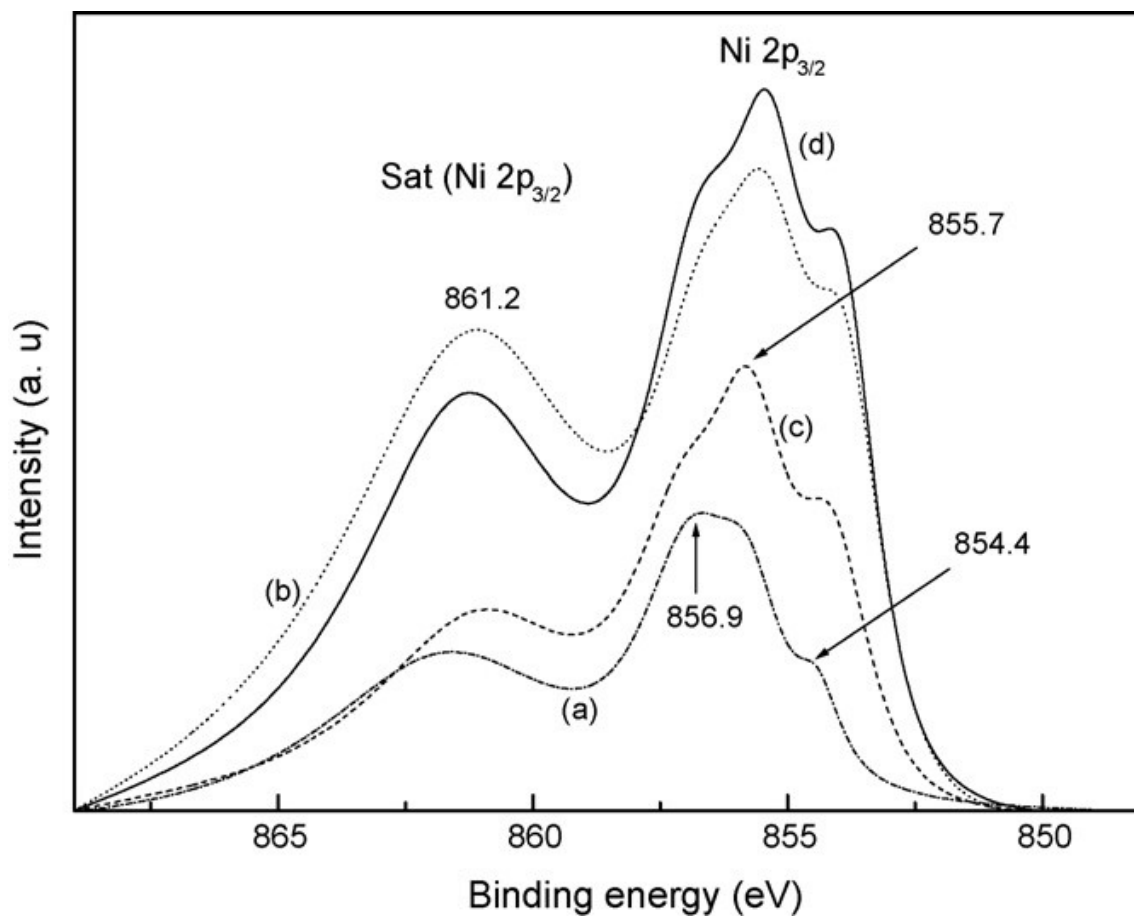
Fig. 5. XPS spectra of Ni 2p$_{3/2}$ region of (a) Ni(1)/CaHAp; (b) Ni(8)/CaHAp; (c) Ni(1)/CaFAp; (d) Ni(8)/CaFAp
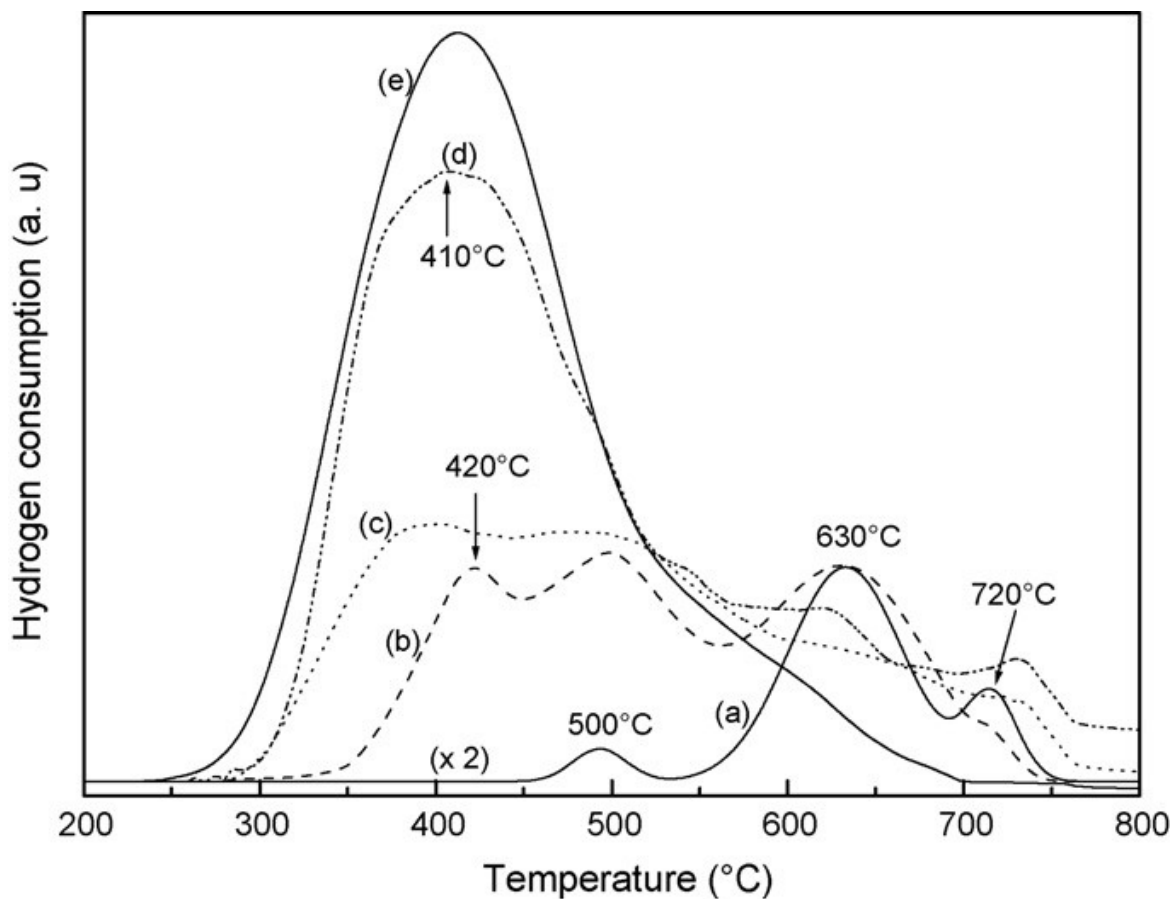
Fig. 6. TPR diagrams of Ni(x)/CaHAp loaded with (a) x = 1%; (b) x = 2%; (c) x = 4%; (d) x = 8%; (e) x = 10%.
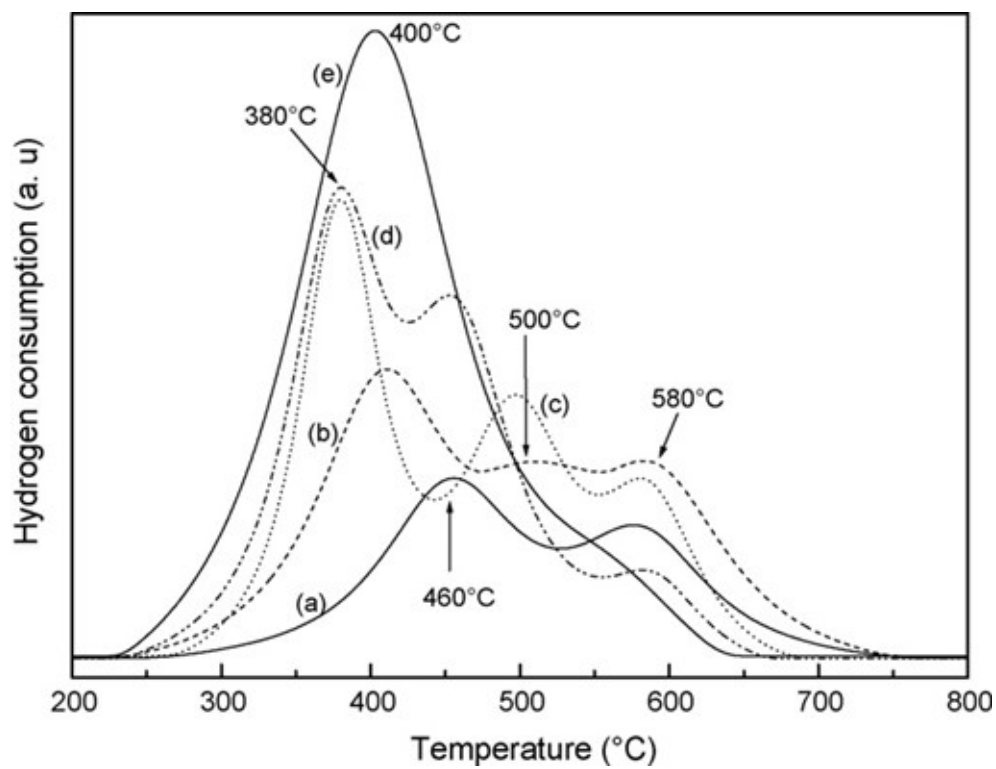
Fig. 7. TPR diagrams of Ni(x)/CaFAp loaded with (a) $x = 1\%$; (b) $x = 2\%$; (c) $x = 4\%$; (d) $x = 8\%$; (e) $x = 10\%$.
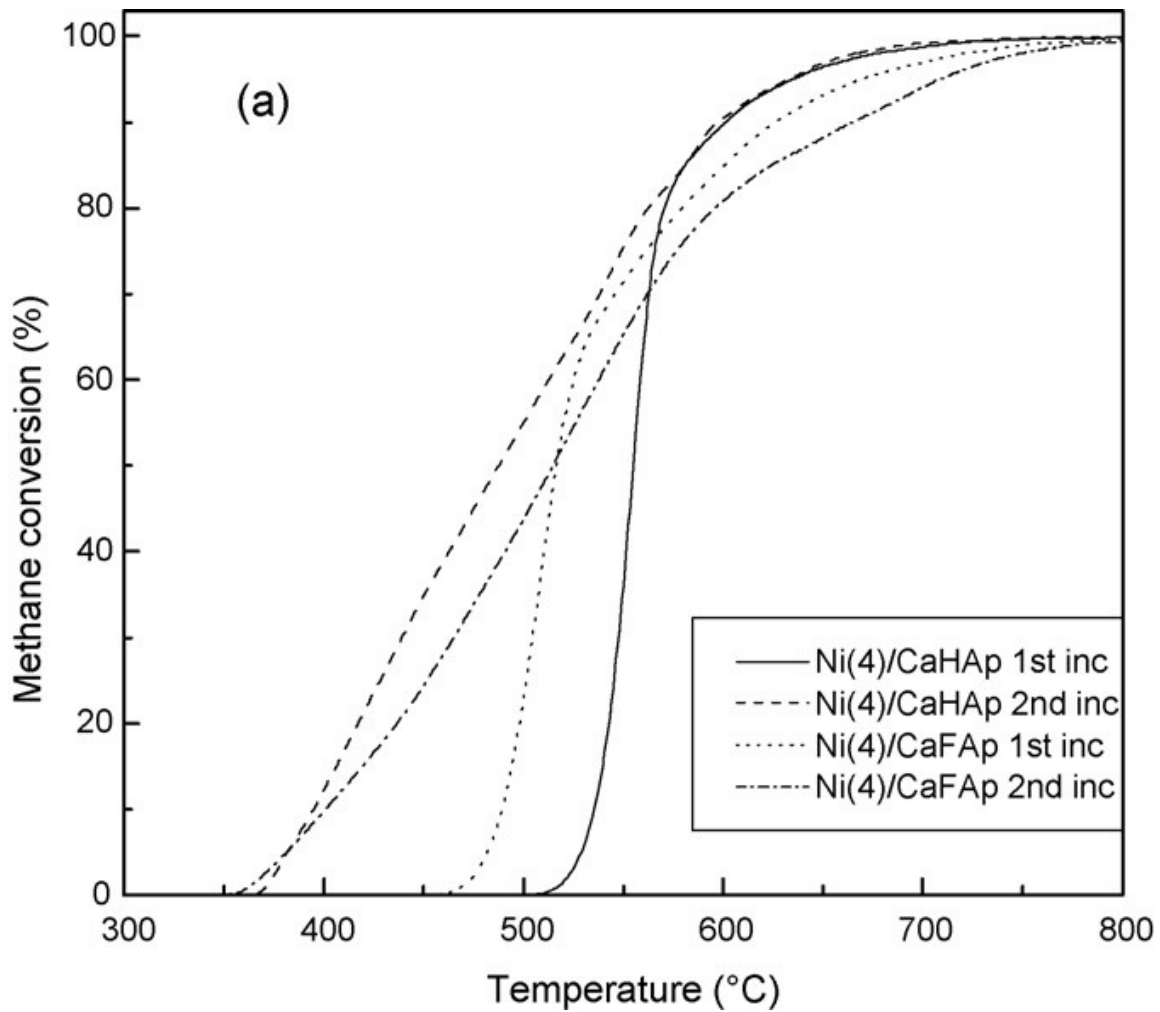
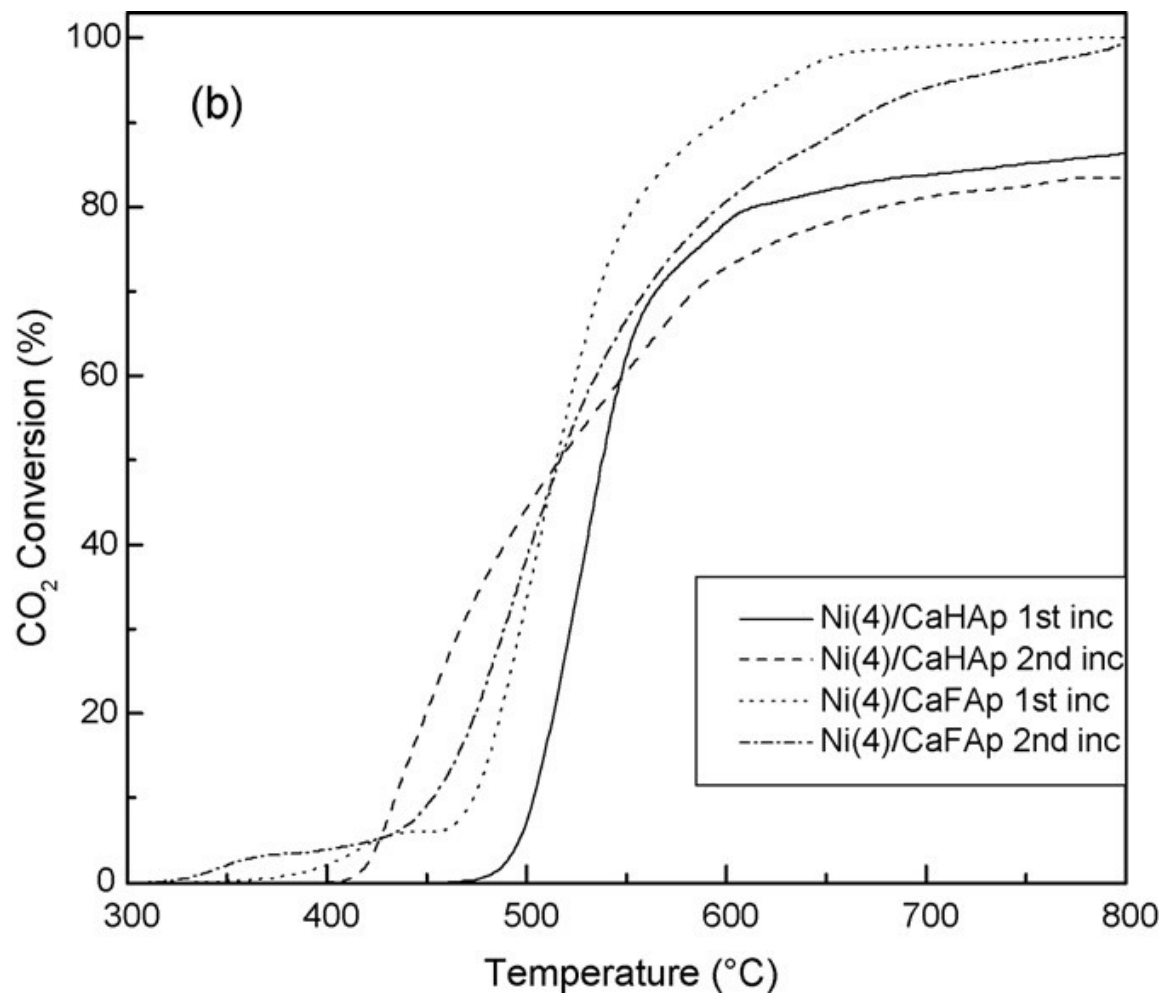Fig. 8. Methane conversion over Ni(4)/CaHAp and Ni(4)/CaFAp vs. the reaction temperature.

Fig. 9. CO_2 conversion over Ni(4)/CaHAp and Ni(4)/CaFAp vs. the reaction temperature.